Colloids and Surfaces A: Physicochemical and Engineering Aspects 681 (2024) 132724

Contents lists available at ScienceDirect

Colloids and Surfaces A: Physicochemical and Engineering Aspects

journal homepage: www.elsevier.com/locate/colsurfa

Low-temperature plasma-induced porous Sb_2WO_6 microspheres with rich oxygen vacancies to promote high-performance photocatalytic activity

Qichang Peng [a,1], Qingdong Ruan [b,1], Bin Wang [a,b,1], Jinyuan Liu [a,b,*], Chao Huang [b], Xingwang Zhu [c], Dan Li [b], Liangliang Liu [b], Yinchuan Wang [b], Xiaolin Zhang [b], Jia Yan [a], Paul K. Chu [b,**], Hui Xu [a,**]

[a] School of the Environment and Safety Engineering, Institute for Energy Research, Jiangsu University, 301 Xuefu Road, Zhenjiang 212013, China
[b] Department of Physics, Department of Materials Science and Engineering, and Department of Biomedical Engineering, City University of Hong Kong, Tat Chee Avenue, Kowloon, Hong Kong, China
[c] College of Environmental Science and Engineering, Yangzhou University, Yangzhou 225009, China

HIGHLIGHTS

- The OV-Sb_2WO_6 materials with oxygen-rich vacancies are formed via low-temperature plasma.
- The introduction of oxygen vacancies facilitates the separation of photo-producted carriers, improving the photocatalytic performance.
- During the photocatalytic process, photogenerated holes(h^+) played a crucial role as the reactive species.

GRAPHICAL ABSTRACT

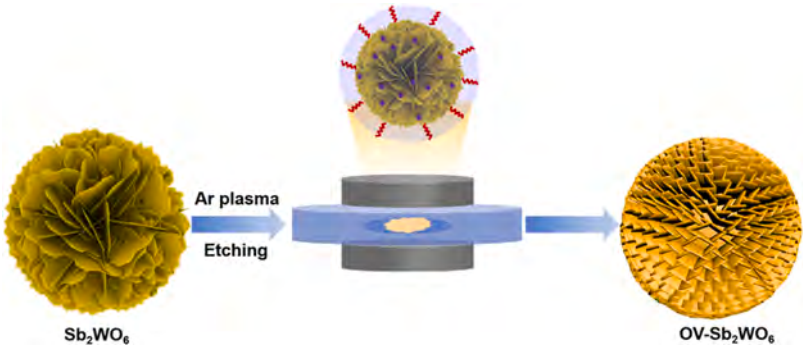

ARTICLE INFO

Keywords:
Sb_2WO_6
Oxygen vacancy
Plasma treatment
Photocatalyst
Degradation

ABSTRACT

The escalating issue of water pollution has sparked significant attention among researchers in the field of photocatalysis. Consequently, it holds immense significance to develop photocatalysts that exhibit high charge separation efficiency and stability for effectively degrading pollutants in water. In this study, OV-Sb_2WO_6-X photocatalyst was synthesized by incorporating oxygen vacancies into pristine Sb_2WO_6. The introduction of oxygen vacancies significantly enhanced the charge separation efficiency, resulting in a substantial improvement in the photocatalytic activity. The content of oxygen vacancies was controlled by plasma treatment time, processed for 10, 20 and 30 min, and electron paramagnetic resonance (EPR) test demonstrated the introduction of oxygen vacancies successfully. Furthermore, X-ray photoelectron spectroscopy (XPS) characterized the internal electron flow direction of the photocatalyst. OV-Sb_2WO_6-20 showed the degradation rate of Rhodamine B (RhB) that nine times of the Sb_2WO_6, while the Tetracyclines (TC) degradation rate showed 3.5 times that of Sb_2WO_6.

* Corresponding author at: School of Chemistry and Chemical Engineering, Institute for Energy Research, Jiangsu University, 301 Xuefu Road, Zhenjiang 212013, China.
** Corresponding authors.
E-mail addresses: jyliu@ujs.edu.cn (J. Liu), paul.chu@cityu.edu.hk (P.K. Chu), xh@ujs.edu.cn (H. Xu).
[1] These authors contributed equally to this work

https://doi.org/10.1016/j.colsurfa.2023.132724
Received 3 August 2023; Received in revised form 13 October 2023; Accepted 3 November 2023
Available online 4 November 2023

Moreover, OV-Sb_2WO_6-20 exhibited superior stability in terms of recycling activity and material structural integrity. Additionally, free radical trapping experiments and electron spin-resonance spectroscopy characterization demonstrated that h^+ played a crucial role as the reactive species during the degradation process. This research presents a viable approach for the modification of Sb_2WO_6-based materials, enabling effective treatment of dye wastewater and achieving successful purification.

1. Introduction

In recent decades, the rapid pace of industrialization has resulted in the discharge of large volumes of industrial wastewater, leading to the deterioration of our water environment [1,2]. Amongst the various types of industrial wastewater, dye wastewater has emerged as a challenging one to treat due to its significant discharge volume, low biodegradability, and high toxicity [3,4]. Traditional methods for sewage treatment have encountered several issues, including high costs, low efficiency and complexity [5]. Therefore, the implementation of photocatalytic technology for treating this printing and dyeing wastewater has gained attention, showcasing efficient and non-toxic outcomes [6]. This advancement is crucial for expanding the scope of practical applications of photocatalysis. In recent years, in the treatment of wastewater containing antibiotics and heavy metals, researchers have mainly constructed S-type heterojunctions with two catalysts, accelerated the flow of electrons and promoted the degradation of photocatalytic pollutants by establishing a built-in electric field [7]. For example, Bi-based materials are widely used in the field of photocatalysis, and Li et al. prepared S-type heterojunction materials by modifying $Cd_{0.5}Zn_{0.5}S/Bi_2MoO_6$ with carbon quantum dots, which can efficiently degrade antibiotics. In addition, Bi_2WO_6, BiOBr, etc. have been constructed heterogeneously, showing great performance improvement in photocatalytic degradation of antibiotic-containing and Cr(VI) wastewater [8].

Semiconductors with Aurivilius structures exhibit excellent electronic conductivity and suitable band gaps, making them highly promising visible light driven photocatalysis [9,10]. Among these materials, Sb_2WO_6 as an Aurivillius-type ternary oxide, has a layered structure consisting of alternatively aligned $(Sb_2O_2)^{2+}$ layer and $(WO_4)^{2-}$ layer [11–14]. Due to its unique laminar structure and physicochemical properties, Sb_2WO_6 have been used in the field of photocatalysis. However, its photointroduced carriers are easy to compound with holes, which severely limits its further development in photocatalysis. As found in previous studies of Sb_2WO_6 materials that superoxide from the reduction reaction pathway and ROS such as hydroxyl radicals from the oxidation reaction pathway play an important role in the degradation of organic pollutants [15]. Since the oxidation and reduction reactions are complementary and mutually restrictive, theoretically promoting either reaction pathway could improve the overall reaction rate [16]. Therefore, improving the separation efficiency of photoelectron and hole is an effective means to improve the rate of photocatalytic degradation of pollutants [17].

Introducing oxygen vacancies on the surface of the catalyst is an effective modification method to improve the catalytic performance [18]. In recent years, oxygen vacancy modification has been used more in Bi-based catalysts, and its composite products are widely used in CO_2 conversion, NO_x reduction and degradation of pollutants, making a contribution to the mitigation of environmental pollution and energy shortage. Gao et al. designed a new ultra-thin porous Bi_2WO_6 with rich surface oxygen vacancies [19]. The photocatalytic degradation of TC activity is about 52.6 times that of the pristine Bi_2WO_6. The main reason is that the introduction of oxygen vacancies increased the adsorption energy of O_2 and enhanced the chemoradsorption of O_2, thus activating O_2 to generate more·O_2^-. Shen et al. prepared oxygen-vacancy catalysts by injecting Cu atoms into a thin monolayer of $Ti_{0.91}O_2$, which highly selectively converted CO_2 into C_3H_8 [20]. The reason for reaching such an effect is that these oxygen vacancies regulate electronic coupled interactions between Ti atoms, where the formation of unique Cu-Ti-VO units in Ti can stabilize and reduce the energy levels of the intermediate, tuning C_1-C_1 and C_1-C_2 coupling to thermodynamically favorable exothermic processes. Wang et al. proposed a photocatalyst constructed from a small (1 mol%) amorphous BiOCl nanosheet assembled on TiO_2 (expressed as 0.01 BOC/TiO_2), which showed excellent performance in the oxidation of toluene to benzene formaldehyde [21]. The amorphous structure of BOC gives it rich surface oxygen vacancies (Ov), which can further promote charge separation. In conclusion, the surface oxygen vacancy of the material has the great advantages of promoting the charge separation, increasing the chemisorption energy, and adjusting the surface charge distribution, which is a relatively simple modification strategy to improve the catalyst performance [22,23].

In this study, OV-Sb_2WO_6-X materials were synthesized using a simple solvent thermal method, followed by the introduction of oxygen vacancies on the catalyst's surface through plasma discharge treatment. It was found that the performance of the photocatalytic degradation of RhB and TC was greatly improved. OV-Sb_2WO_6-20 showed the degradation rate of RhB that nine times of the Sb_2WO_6, while the TC degradation rate showed 3.5 times that of Sb_2WO_6. Combining electron spin resonance spectroscopy characterization and radical trapping experiments proposed the degradation of pollutant pathway, where h^+,·OH, $^1O_2$ play a major role as a reactive material in the degradation process. The introduction of oxygen vacancies suppresses the combination of photogenerated electrons and holes, which allows the electron to produce more superoxide radicals from reduction reaction pathway of the photocatalyst and accelerates the h^+ to guide two-step generation of singlet oxygen and hydroxyl radicals. Furthermore, the structural and photochemical properties of Sb_2WO_6 materials were characterized by experimental techniques including XRD, UV–vis DRS, and XPS, and the presence of oxygen vacancies was demonstrated by EPR and other tests.

2. Experimental

2.1. Reagents

Antimony trichloride ($SbCl_3$, 99 %) and sodium tungstate dihydrate ($Na_2WO_4{\cdot}2\ H_2O$, 99.5 %) were obtained from Aladdin Chemistry. (Shanghai, China). Ethanol (99 %), Triethanolamine (TEOA, 99 %), isopropanol (IPA, 99.7 %), 1,4-benzoquinone (BQ, 98 %) and l-tryptophan were received from Sinopharm Chemical Reagent. (Shanghai, China). In this experiment, deionized water was used whenever any unstated solution.

2.2. Preparation of Sb_2WO_6 and OV-Sb_2WO_6

Sb_2WO_6 was synthesized by solvothermal method using the ethanol and H_2O as the solvent. 0.228 g of $SbCl_3$ and 0.165 g of $Na_2WO_4{\cdot}2\ H_2O$ were dispersed in 15 mL of ethanol and in 15 mL of H_2O, respectively. The sodium tungstate solution was then added successively to the antimony trichloride solution. After continuous stirring for 30 min, adjusting the mixed solution pH to 2, then pouring into 50 mL Teflon-lined autoclave, which was heated and maintained at 180 °C for 12 h. Next, the precipitates were centrifuged after two hours later, repeatedly washed with ethanol and water, and dried at 60 °C to obtain Sb_2WO_6. 50 mg of antimony tungstate was dissolved in anhydrous ethanol, sonicated for 30 min to disperse evenly, then coated on quartz glass sheets and dried with a xenon lamp. The quartz glass sheet was put into the

dielectric blocking reactor, evenly fed into the gas, and the current voltage was applied for plasma discharge. After the treatment by 10/20/30 min later, a defective antimony tungstate photocatalyst was obtained, named as OV-Sb_2WO_6-10, OV-Sb_2WO_6-20 and OV-Sb_2WO_6-30. The specific flow chart is shown in the Scheme 1.

2.3. Measurement of photocatalytic properties

The performance of the Sb_2WO_6 on photodegraded pollutants was assessed with 10 mg/L RhB as the target contaminant. Weigh 25 mg of photocatalyst was added to the glass photocatalytic reactor, and then 50 mL of 10 mg/L RhB solution was added to the reactor. A 250 W Xe arc lamp with an appropriate UV cut-off filter ($\lambda > 400$ nm) was used as the light source for this study, and the experimental temperature was kept at 30 ℃ by using a thermostatic circulating water system to effectively avoid the influence of thermal catalysis on this experiment. Before turning the light source on to start the photocatalytic reaction, the suspension mixed with the target pollutant and the photocatalyst was sonicated uniformly and magnetically stirred in the dark to achieve adsorption-desorption equilibrium. At a certain time interval, 3 mL of the solution was sampled using a syringe and immediately centrifuged and filtered out of the catalyst particles for subsequent analysis. The concentration of Rhodamine B(RhB) and Tetracyclines(TC) was measured by a UV–vis spectrophotometer (UV-1800, Shimadzu, Japan) by checking its maximum absorption wavelength at 553 and 356 nm. The K value is evaluated by the following equation:

$$-kt = \ln\frac{C_t}{C_0}$$

where the C_t is the pollution concentration at the reaction time of t min, C_0 is the pollution concentration after dark reaction.

2.4. Characterization of materials

The X-ray diffraction (XRD) patterns were using Shimadzu XRD-6100 with Cu Ka radiation in the range of 2θ from 10° to 80°. X-Ray photoelectron spectroscopy (XPS) measurements were tested on VG MultiLab 2000 system with a monochromatic Mg-Kα source operated at 20 kV. The morphologies were characterized by Transmission electron microscopy (TEM) (JEOL JEM-2010 microscope) at an accelerating voltage of 200 kV and Scanning electron microscopy (SEM) (JSM-7800 F microscope). Shimadzu UV-2450 spectrophotometer were used to record the diffuse reflection spectra (DRS) of the prepared samples in the range of 200–800 nm with solid $BaSO_4$ slices as the reference. Electron spin resonance (ESR) spectra were conducted on a Bruker model ESR JES-FA200 spectrometer. The electrochemical impedance spectroscopy (EIS) and photocurrents were measured on a CHI660B electrochemical system.

3. Results and discussion

3.1. Characterizations

3.1.1. Morphologies of photocatalysts

The surface morphology of the prepared samples was analyzed using SEM and TEM. Fig. 1a-b presents the SEM of the pristine Sb_2WO_6 images at different magnification. It can be observed that the pristine Sb_2WO_6 sample consists of uniformly shaped spheres. A single sphere within the pristine Sb_2WO_6 sample consists of multiple nanosheets arranged in a three-dimensional hierarchical structure. To further confirm the layered structure of the nanosheets, Fig. 1c shows a TEM (HRTEM) image inset of a single pristine Sb_2WO_6 sphere (Fig. 1b). The HRTEM image clearly reveals lattice fringes at the edge, indicating a well-defined crystal phase structure with a lattice spacing of 0.33 nm in the Sb_2WO_6 sphere, consistent with the (211) crystal surface spacing of the standard Sb_2WO_6. Fig. 1d-f depict the SEM and TEM images of the plasma-treated OV-Sb_2WO_6-20 sample, respectively, which exhibit the same size and three-dimensional structure as the pristine Sb_2WO_6. The lattice fringes in the images have a spacing of 0.44 nm, corresponding to the (111) crystal surface [18]. The only distinction from the pristine Sb_2WO_6 is the slightly roughened nanosheet surface, attributed to the successful introduction of oxygen vacancies through Ar etching.

Fig. 2a displays the XRD patterns of the pristine Sb_2WO_6 and OV-Sb_2WO_6-20 with different durations of Ar plasma treatment. The peaks observed at 20.1°, 26.80°, 32.78°, 36.49°, 40.22°, 47.33°, 49.81° and 53.27° correspond to the characteristic peaks of triclinic phase Sb_2WO_6 (JCPDS No. 50–1553) [24]. Importantly, the characteristic diffraction peaks of OV-Sb_2WO_6-20 show no significant shift, indicating that the crystal structure of material remains unchanged after the simple plasma treatment. Notably, the XRD peak intensity of the treated OV-Sb_2WO_6-20 is higher to the other treated materials, approaching the peak intensity of the pristine Sb_2WO_6. This straightforward modification method enables the rapid preparation of the desired materials.

The chemical composition and valence states of the materials were analyzed by XPS [25]. The peaks observed at 284.78 eV (Fig. 2b) are assigned to the C 1 s and serve as a reference. The high-resolution XPS spectra of the aforementioned elements are presented in Figs. 2c–2e. The Sb 3d signal in Sb_2WO_6 was deconvoluted to Sb $3d_{3/2}$ and Sb $3d_{5/2}$, corresponding to the binding energies of 539.8 eV and 530.5 eV, respectively (Fig. 2c) [26]. The W 4 f spectra of Sb_2WO_6 can be deconvoluted to the peaks of $W^{6+}4f_{5/2}$, $W^{5+}4f_{7/2}$, $W^{6+}4f_{7/2}$ and $W^{5+}4f_{5/2}$, correspond to binding energies of 37.8 eV, 34.4 eV, 35.6 eV and 36.0 eV (Fig. 2d) [11,27]. As shown in Fig. 2e, the O 1s spectrum shows a peak at 530.5 eV, but the detailed attributed is challenging due to the overlapping the interweaving of the Sb 3d and O 1 s binding energy ranges (526–534 eV) [9]. The O 1 s spectra can be deconvoluted into W-O, Sb $3d_{5/2}$ and Sb-O peaks, corresponding to binding energies of 530.2 eV,

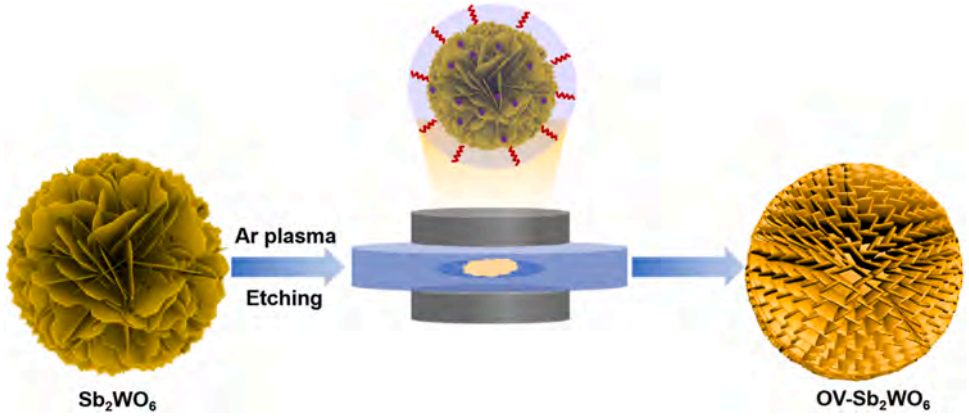

Scheme 1. Schematic illustration of Sb_2WO_6 with oxygen vacancies by Ar plasma treatment.

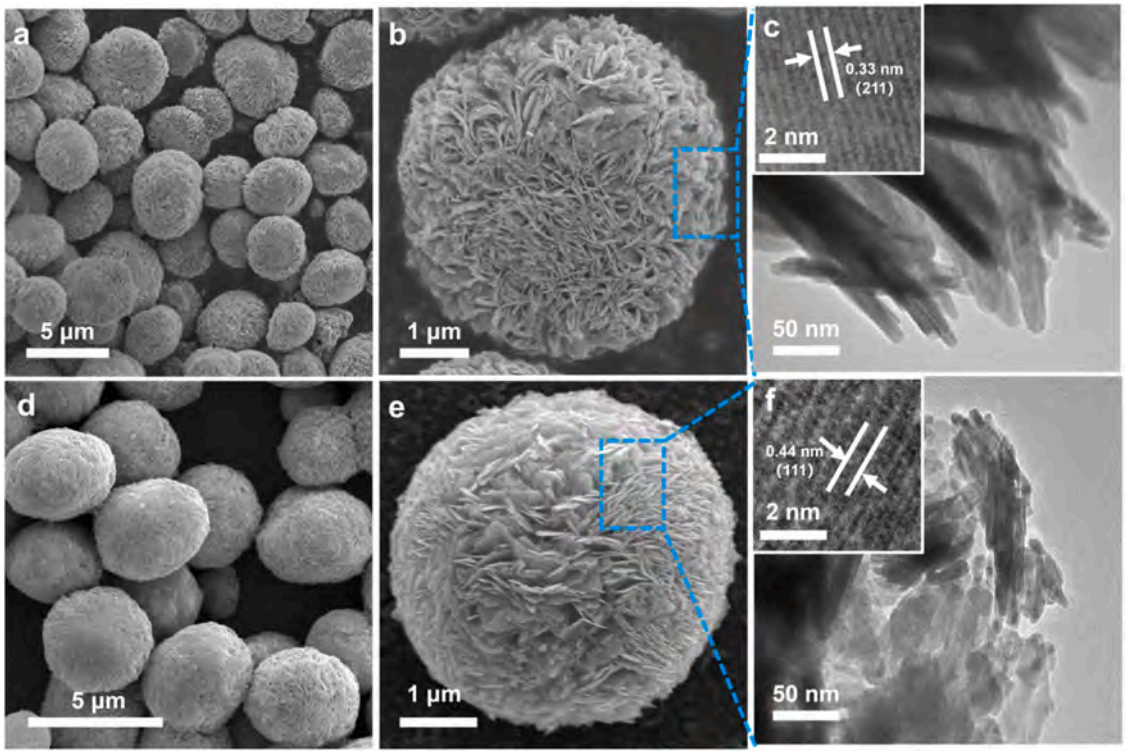

Fig. 1. (a, b) SEM images, (c) TEM and HRTEM images of pristine Sb_2WO_6 nanostructures; (d, e) SEM images, (f) TEM and HRTEM images of OV-Sb_2WO_6-20 nanostructures.

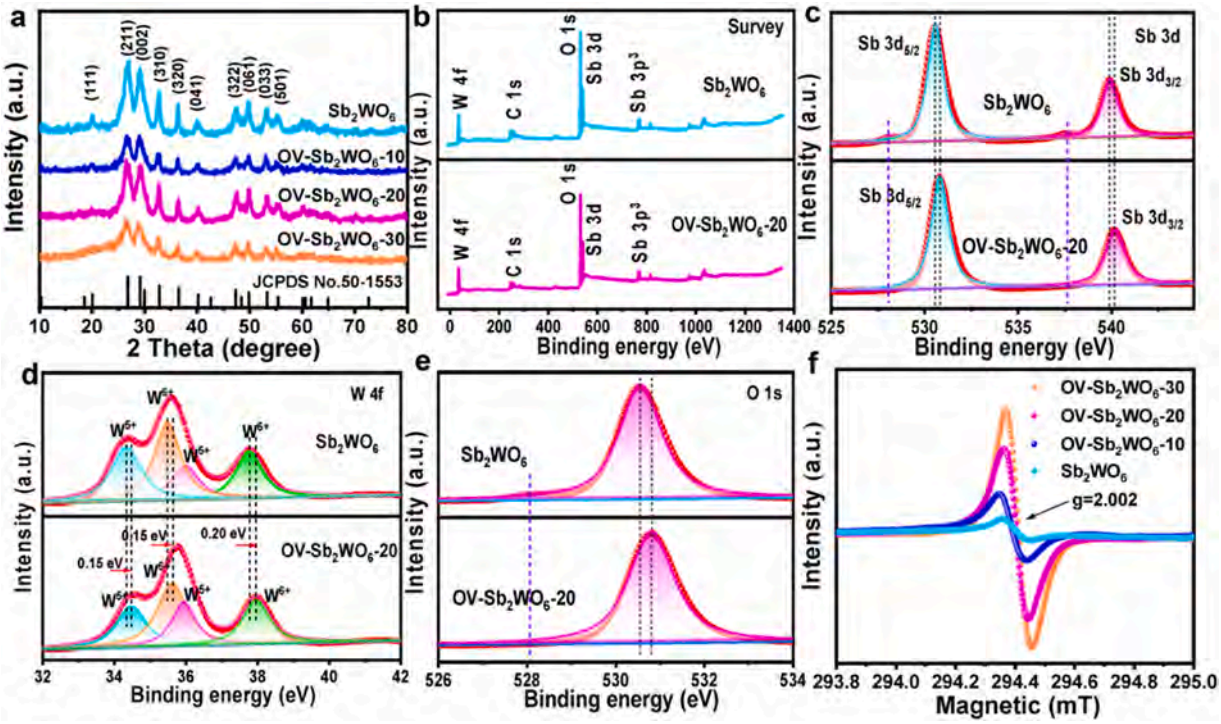

Fig. 2. (a) XRD patterns of as-prepared samples; (b) high-resolution XPS spectra of as-prepared samples survey, (c) Sb 3d, (d) W 4 f, and (e) O 1 s; (f) EPR spectra of as-prepared samples.

530.5 eV and 530.9 eV, respectively [27,29]. In particular, the characteristic peak belonging to the lattice oxygen at 528.2 eV disappeared on the O 1s spectra of OV-Sb_2WO_6-20, indicated that the lattice oxygen escaped upon plasma treatment. Importantly, the Sb, O, and W peaks in the OV-Sb_2WO_6-20 sample show a red shift compared to the pristine Sb_2WO_6, suggesting that the presence of oxygen defects impacts electron transfer. This suggests that some W^{6+} atoms in Sb_2WO_6 are reduced to W^{5+} due to the formation of oxygen vacancies. To further demonstrate

the elevated concentration of oxygen vacancies in the catalyst due to plasma treatment, analysis of EPR spectra was conducted. As depicted in Fig. 2f, both OV-Sb_2WO_6-20 and Sb_2WO_6 exhibit an EPR signal at g= 2.002, corresponding to a single electron captured in an oxygen vacancy [28,30]. The signal intensity of OV-Sb_2WO_6-20 is significantly enhanced compared to the original Sb_2WO_6, providing evidence that the plasma treatment effectively increases the oxygen vacancy concentration in the catalyst.

In Fig. 3a, a diagram depicted the sample treated with plasma for various durations under an Ar atmosphere, revealing that the color of the sample surface becomes brighter with increasing plasma treatment time [20]. Based on the aforementioned EPR tests, it can be inferred that the escape velocity of the oxygen atoms on the surface of the photocatalyst occurs more frequently. The optical absorption of the Sb_2WO_6 samples was measured with a UV–vis diffuse reflectance spectrometer [31,32] (Fig. 3b). All prepared samples exhibited robust absorption in the UV and visible regions, with absorption band edges around 550 nm. The light absorption intensity of OV-Sb_2WO_6-20 did not change too much, indicating that the introduced oxygen vacancy does not change its bandgap size. The band gaps of the pristine Sb_2WO_6 and OV-Sb_2WO_6-20 are 2.12 eV and 2.14 eV, respectively (Fig. 3**c**), which are suitable for the photocatalytic reaction. Mott-Schottky plots of Sb_2WO_6 and OV-Sb_2WO_6-20 samples were used to evaluated the effect on charge carrier concentration. As shown in Fig. 3d and e, the flat potential (E_{FB}) for Sb_2WO_6 and OV-Sb_2WO_6-20 is − 0.60 V and − 0.61 V (relative to Ag/AgCl (pH=6.8)). The E_{FB} measured using the Ag/AgCl reference electrode can be converted to a normal hydrogen electrode (NHE) potential using the following equation [32,34]:

$$E_{FB} = E_{Ag/AgCl} + 0{\cdot}059\ pH + E^0_{Ag/AgCl},$$

where the electrolyte pH is 6.8 and $E^0_{Ag/AgCl}$ is 0.197 eV. Thus, E_{FB} value of Sb_2WO_6 and OV-Sb_2WO_6-20 are calculate as − 0.00 and − 0.01 vs. NHE. In addition, for n-type semiconductors, the E_{CB} is very close to the (negative voltage increase −0.3 V) E_{FB}. Thus, the E_{CB} values for Sb_2WO_6 and OV-Sb_2WO_6-20 are equivalent to − 0.30 and − 0.31 V vs. NHE. Respectively. Combined with the UV–vis DRS, the corresponding E_{VB} values for Sb_2WO_6 and OV-Sb_2WO_6-20 were calculated as 1.82 and 1.83 eV vs. NHE. Schematic diagram of the energy band structure of as-prepared samples is shown in the Fig. 3f.

To further investigate the impact of oxygen vacancies on the separation of photogenerated electrons and holes, the photoelectric properties of Sb_2WO_6 and OV-Sb_2WO_6-20 were also measured [23]. The photocurrent curves of the pristine Sb_2WO_6 and OV-Sb_2WO_6-20 were presented in Fig. 3g. It can be observed that OV-Sb_2WO_6-20 demonstrates a higher photocurrent density compared to Sb_2WO_6 upon photoexcitation, suggesting a greater efficiency in the separation of photogenerated electron-hole pairs [33]. Furthermore, the charge transfer in the photocatalyst was evaluated using the EIS Nyquist plot [34]. As depicted in Fig. 3h, the Nyquist diagram of OV-Sb_2WO_6-20 exhibits a smaller minimum arc radius in comparison to pristine Sb_2WO_6, indicating a lower charge transport resistance in OV-Sb_2WO_6-20 [22,35]. This lower resistance facilitates the transfer of photogenerated electrons and holes from the bulk of the sample to its

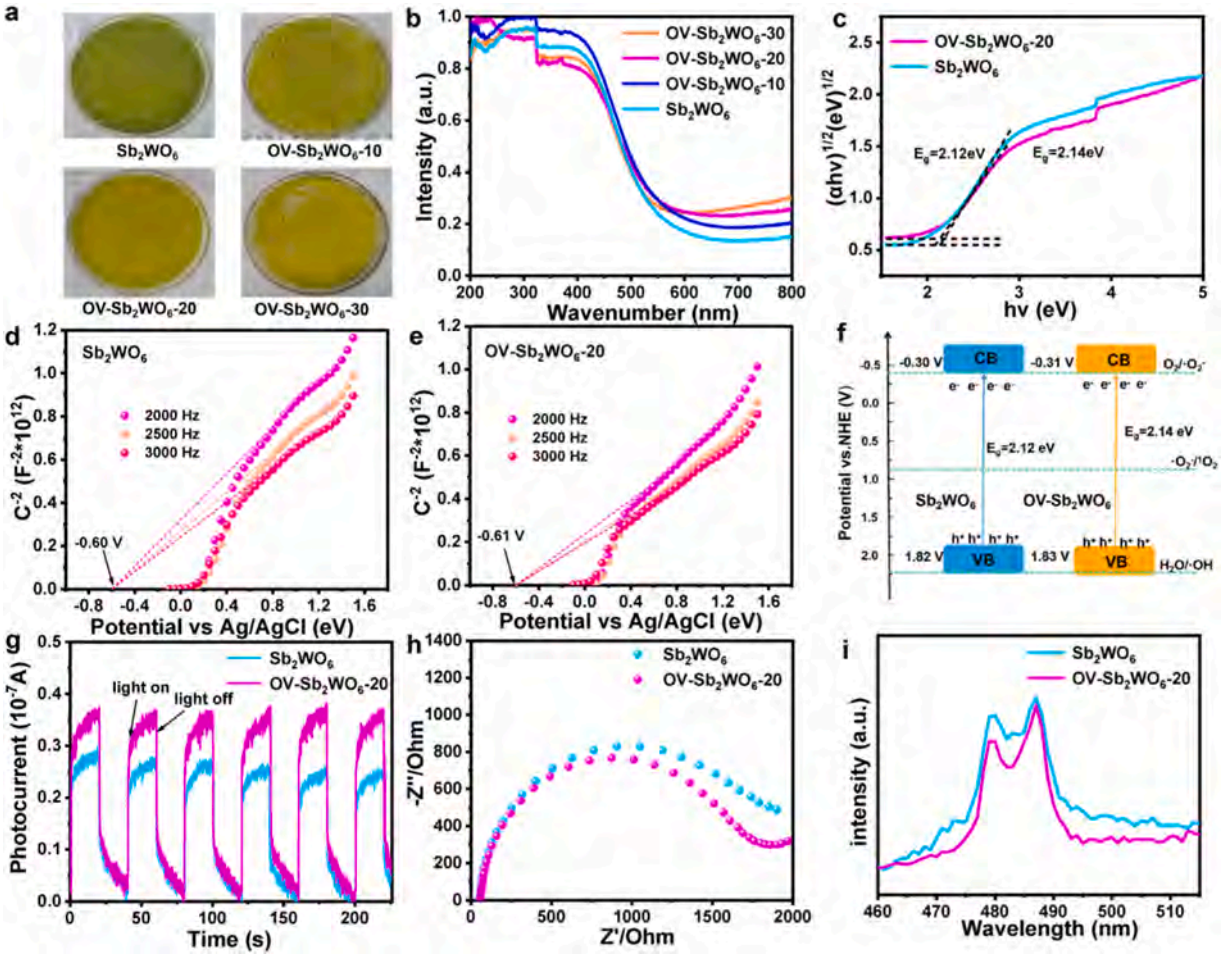

Fig. 3. (a) physical diagram of the as-prepared samples; (b) UV–vis diffuse reflection spectra of the as-prepared samples; (c) $(ahv)^{1/2}$ versus hv plots, (d) VB spectra and (e) Mott-Schottky plots of as-prepared samples; (f) Schematic diagram of the energy band structure of as-prepared samples; (g) Photocurrent responses; (h) Electrochemical impedance spectra Nyquist curves and (i) Room-temperature PL spectra of prepared samples.

surface. In addition, photoluminescence (PL) was performed to characterize the radiative recombination process of photoexcited carriers, which demonstrated the efficiency of carrier separation in a photocatalyst [36]. Fig. 3i displays the PL spectra of Sb_2WO_6 and OV-Sb_2WO_6-20 excited at a wavelength of 310 nm. The PL intensity of OV-Sb_2WO_6-20 is observed to be weaker than that of the pristine Sb_2WO_6, indicating that OV-Sb_2WO_6 has lower electron and hole recombination rates [37,38]. Above characterization results indicated that the separation efficiency of photogenerated electron-hole pairs of samples with oxygen vacancies by plasma treatment was improved.

3.2. Photocatalytic activity evaluation

RhB as a common organic pollutant, was selected as a target contaminant in this experiment to assess the photocatalytic performance of Sb_2WO_6 materials. As shown in Fig. 4a, RhB solution was photodegraded in the absence of a catalyst and it was found that there was no degradation effect, indicating that the catalyst was the primary substance contributing to degradation. Moreover, the adsorption performance of the catalyst was tested under dark conditions, as shown in Fig. S1, demonstrating that the adsorption effect was not obvious and did not affect the degradation reaction. The catalytic degradation of RhB under visible light was less than 20 % within 6 h by pristine Sb_2WO_6. In contrast, the OV-Sb_2WO_6-20 material showed a huge improvement in degradation performance, with the degradation rate of RhB arrived at 72%, which was much higher than that of OV-Sb_2WO_6-10 (60 %) and OV-Sb_2WO_6-30 (55 %). To further quantitatively evaluate the photocatalytic activity of the different photocatalysts, the kinetic curves were recorded in Fig. 4b. Clearly, the k value of OV-Sb_2WO_6-20 (0.27 h^{-1}) is 9 times of Sb_2WO_6 (0.03 h^{-1}), and 1.6 times that of OV-Sb_2WO_6-10 (0.168 h^{-1}), and 2 times that of OV-Sb_2WO_6-30 (0.126 h^{-1}), respectively (Fig. 4c). Here, we also make table statistics on the performance improvement multiple of different catalysts after modification, as shown in Table S1, indicating that the performance improvement of Sb_2WO_6 is relatively large. The reason why the degradation performance of OV-Sb_2WO_6-20 is better than the other two plasma-treated samples is that the introduction of less oxygen vacancies will enhance the charge separation capacity less, while the introduction of excessive oxygen vacancies will affect the surface structure of the photocatalyst [6,20]. In addition, TC was selected as an additional target pollutant to continue to evaluate the performance of the photocatalyst. Fig. 4d-f shows the activity of the degraded TC, the kinetic curve and the first-order kinetic constant k-value plot [39]. During the same time period, OV-Sb_2WO_6-20 exhibited the highest photodegradation effect, with a degradation rate 3.5 times faster than pristine Sb_2WO_6, 1.6 times faster than OV-Sb_2WO_6-10, and 1.4 times faster than OV-Sb_2WO_6-30. The k value of pristine Sb_2WO_6, OV-Sb_2WO_6-10, OV-Sb_2WO_6-20 and OV-Sb_2WO_6-30 is 0.036, 0.072, 0.126 and 0.084 h^{-1}, which all corresponding the result of degrading RhB.

The photocatalytic stability of the best sample was investigated by

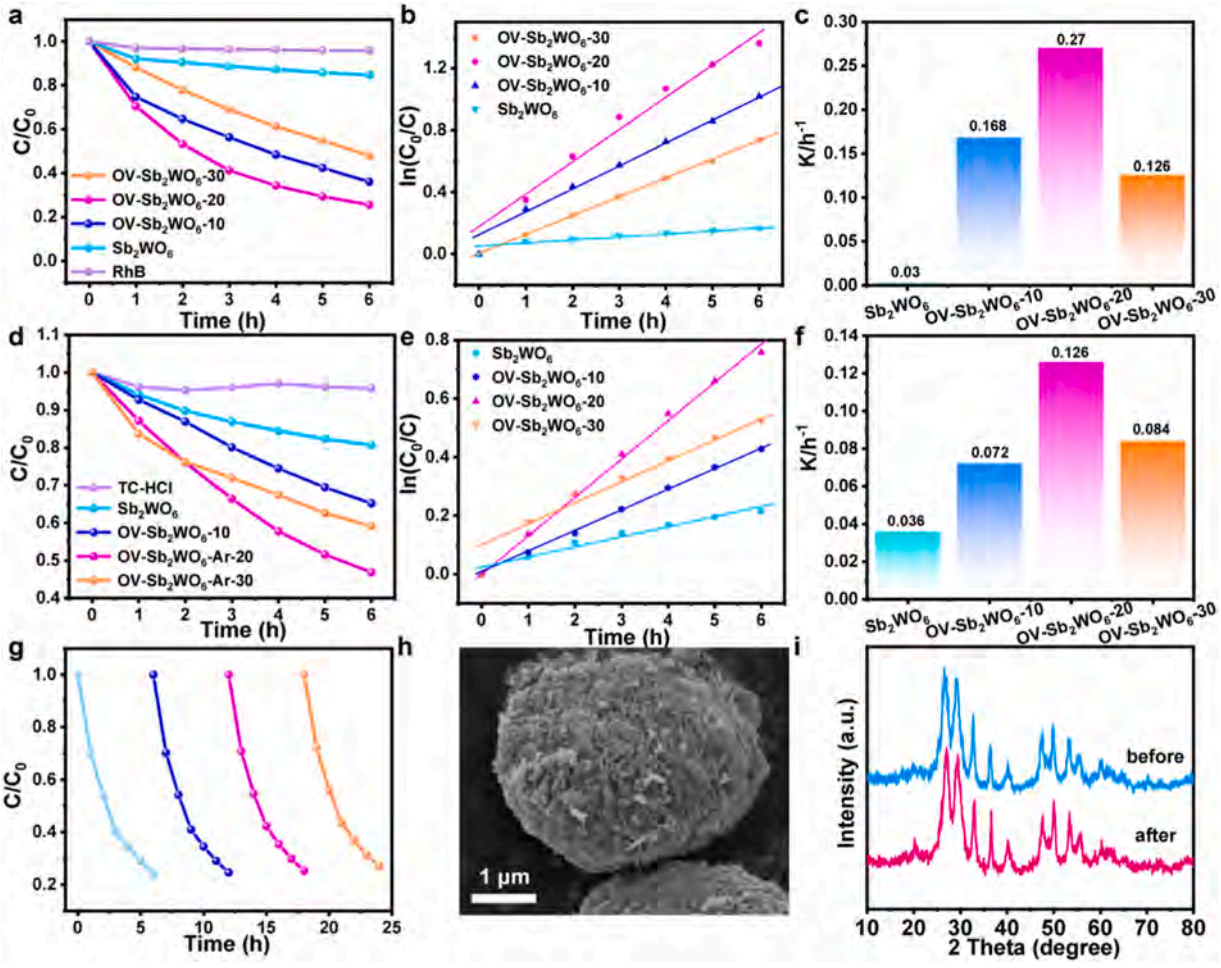

Fig. 4. (a) Photocatalytic degradation of RhB; (b) Pseudo-first-order kinetics for the degradation of RhB by different photocatalysts under visible light irradiation; (c) K value of degrading RhB by as-prepared samples; (d) Photocatalytic degradation of TC; (e) Pseudo-first-order kinetics for the degradation of TC by different photocatalysts under visible light irradiation; (f) K value of degrading TC by as-prepared samples; (g) Photocatalytic recycling test; (h) SEM and (i) XRD spectra of OV-Sb_2WO_6-20 after recycling test.

cycling experiments under visible light. As shown in Fig. 4g, OV-Sb_2WO_6-20 samples showed essentially catalytic activity after four cycles, indicating excellent photocatalytic stability of the material. The SEM showed that the structure was still spherical, with no chemical change in the solution. The structure of the materials after the cycle was used XRD to experiment. As shown in Fig. 4**i**, the characteristic signals intensity of OV-Sb_2WO_6-20 sample has no significant change after four cycle tests, and no signal peaks belonging to Sb_2WO_6 have disappeared, demonstrating the strong structural stability of the materials.

Furthermore, to explore the mechanism of RhB degradation by Sb_2WO_6 photocatalysts, radical trapping experiments were performed. The study chosen EDTA, BQ, IPA and l-tryptophan as scavengers of h^+, $\cdot O_2^-$, ·OH and $^1O_2$, respectively [22]. As shown in the Fig. 5a, the degradation rate of RhB was significantly inhibited by the addition of EDTA, indicating that h^+ play a major role in the degradation process. The photocatalytic degrade RhB performance of OV-Sb_2WO_6-20 was also affected slightly when l-tryptophan, p-benzoquinone and IPA were added, demonstrating that $^1O_2$, $\cdot O_2^-$ and ·OH exhibit second roles in this system [40]. The ESR test was further used to illuminate the type of the active species. In Fig. 5b-e, characteristic signals of $\cdot O_2^-$, ·OH and $^1O_2$ were absent in pristine Sb_2WO_6 and OV-Sb_2WO_6-20 samples under darkness. The characteristic peaks of ·OH, $\cdot O_2^-$ and $^1O_2$ were observed in pristine Sb_2WO_6 and OV-Sb_2WO_6-20, indicating that ·OH, $\cdot O_2^-$ and $^1O_2$ active substances can be produced under light conditions. Notably, the response characteristic peak signal intensity of OV-Sb_2WO_6-20 samples was significantly larger than the pristine Sb_2WO_6, indicating rapid production of active species [41]. Furthermore, the signal peaks in Fig. 5b correspond to the production of light-generated holes, and the signal intensity of h^+ is significantly weakened under visible light irradiation, indicating that the holes are continuously consumed as the reaction occurs. Because the potential of $OH^-/\cdot OH$ (2.40 V vs. NHE) is more correct than the valence bands of both OV-Sb_2WO_6-20 and Sb_2WO_6, ·OH cannot be formed under visible light irradiation, but ·OH can also be generated by a two-step reaction of $\cdot O_2^-$. Thus, the enhanced photocatalytic performance of OV-Sb_2WO_6-20 can be attributed to the introduction of oxygen vacancies, which accelerates the separation of photogenic electron-hole pairs during the reaction.

When EDTA was added, the degradation effect was found to decrease sharply, indicating that the main active substance is h^+, and the production process of ·OH could be attributed to the following reactions : .

$$OV\text{-}Sb_2WO_6\text{-}20 + h\nu \rightarrow e^- + h^+$$

$$O_2 + e^- \rightarrow \cdot O_2^-$$

$$\cdot O_2^- + h^+ \rightarrow {}^1O_2$$

$$O_2 + h\nu \rightarrow {}^1O_2$$

$$\cdot O_2^- + e^- + 2\,h^+ \rightarrow H_2O_2$$

$$H_2O_2 + e^- \rightarrow \cdot OH + OH^-$$

In conclusion, combining the results of ESR and radical trapping tests showed that OV-Sb_2WO_6-20 produced more active species in the photocatalytic degradation of RhB than in Sb_2WO_6 alone. The photocatalytic mechanisms of OV-Sb_2WO_6-20 catalyst were proposed by the above analysis results, and Fig. 5f exhibited the diagrammatic sketch. The electrons in the ground state are excited by visible light, separated from the holes, and form light-generated holes and light-generated electrons in the valence and conduction bands, respectively. Electrons on the CB of Sb_2WO_6 can react with O_2 to form the $\cdot O_2^-$. Under visible light illumination, photoinduction of Sb_2WO_6 surface in situ generates photoelectron hole pairs, and photoelectron transfer to the surface with surrounding oxygen molecules to form ·OH, $^1O_2$ and $\cdot O_2^-$. The h^+, $^1O_2$, $\cdot O_2^-$ and ·OH generated during photocatalysis effectively removed RhB and TC.

4. Conclusion

In this study, the OV-Sb_2WO_6 photocatalyst with oxygen vacancies was synthesized based on the synthesis of Sb_2WO_6 materials using plasma treatment under Ar atmosphere. The introduction of oxygen vacancies on the surface of the catalyst accelerated the separation efficiency of photoproduct carriers. The degradation rate of RhB and TC by OV-Sb_2WO_6-20 was 9 times and 3.5 times to that of pristine Sb_2WO_6 under visible light. Free radical capture experiments show that h^+ was

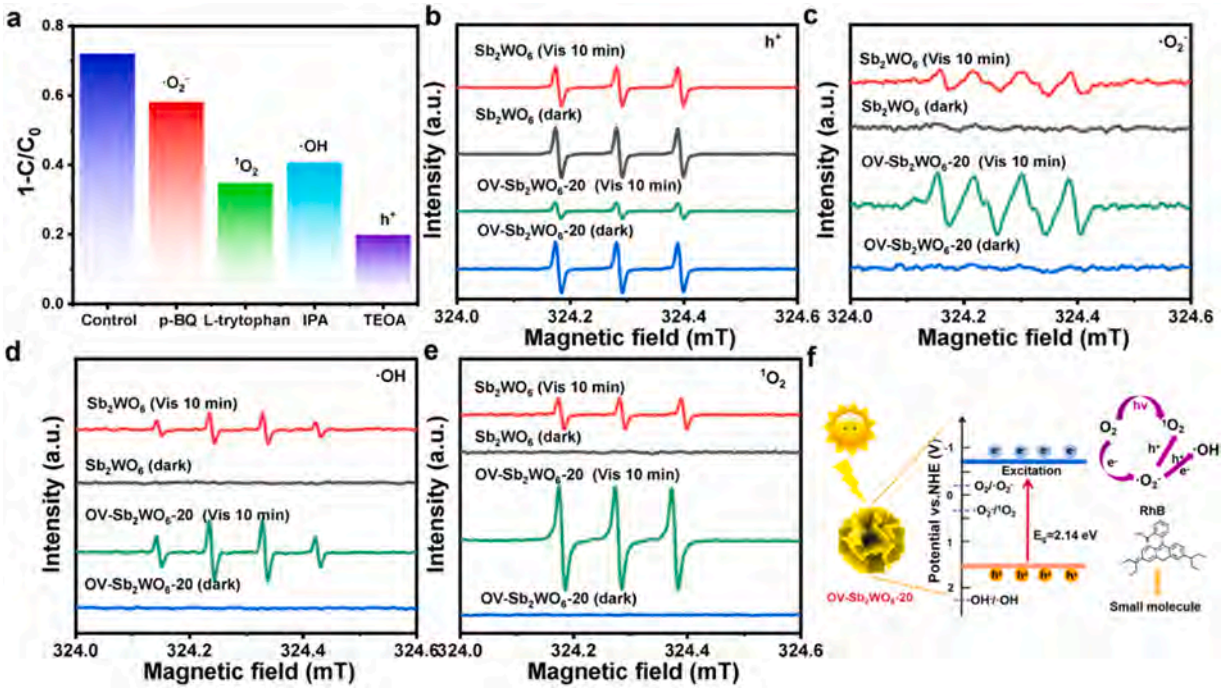

Fig. 5. (a) Trapping experiment of RhB over OV-Sb_2WO_6-20, ESR spectra of radical species (b) h^+, (c) •O_2^-, (d) •OH and (e) $^1O_2$ with pristine Sb_2WO_6 and OV-Sb_2WO_6-20; (f) Mechanism spectra of the degradation of RhB by OV-Sb_2WO_6-20 catalyst.

the main active species during degradation. The efficiency of RhB removal did not change substantially after four cycle tests, demonstrating the stability of the degradation effect of OV-Sb_2WO_6-20. The circulating samples were tested for XRD and SEM, and the sample structure was not broken and had good structural stability. This work demonstrates that the defective regulation design of Sb_2WO_6 materials is feasible to improve the performance of pollutants in degraded water.

CRediT authorship contribution statement

Qichang Peng: Conceptualization, Data curation, Investigation, Writing - original draft. **Qingdong Ruan:** Conceptualization, Writing-review & editing, Supervision. **Bin Wang:** Conceptualization, Resources, Writing-review & editing, Supervision. **Jinyuan Liu:** Data curation, Resources, Investigation, Writing-original draft. **Chao Huang:** Data curation, Investigation. **Xingwang Zhu:** Data curation, Investigation. **Dan Li:** Data curation, Investigation. **Liangliang Liu:** Data curation, Investigation. **Yinchuan Wang:** Data curation, Investigation. **Xiaolin Zhang:** Data curation, Investigation. **Jia Yan:** Data curation, Writing-review & editing. **Paul K. Chu:** Conceptualization, Resources, Writing-review & editing, Supervision. **Hui Xu:** Resources, Writing - review & editing, Supervision.

Declaration of Competing Interest

The authors declare that they have no known competing financial interests or personal relationships that could have appeared to influence the work reported in this paper.

Data availability

No data was used for the research described in the article.

Acknowledgments

This study was financially supported by the National Natural Science Foundation of China (22008095, 22108106, 22308300), China Postdoctoral Science Foundation (No. 2020M680065), Natural Science Foundation of Jiangsu Province (BK20190981, BK20220598), Hong Kong Scholar Program (No. XJ2021021), Key Laboratory of Electrochemical Energy Storage and Energy Conversion of Hainan Province (KFKT2021006, KFKT2022001), City University of Hong Kong Donation Research Grant (DON-RMG No. 9229021), City University of Hong Kong Strategic Research Grant (SRG No. 7005505), as well as City University of Hong Kong Donation Grant (No. 9220061).

Appendix A. Supporting information

Supplementary data associated with this article can be found in the online version at doi:10.1016/j.colsurfa.2023.132724.

References

[1] W. Li, Z. Wang, Y. Li, J.B. Ghasemi, J. Li, G. Zhang, Visible-NIR light-responsive 0D/2D CQDs/Sb_2WO_6 nanosheets with enhanced photocatalytic degradation performance of RhB: unveiling the dual roles of CQDs and mechanism study, J. Hazard Mater. 424 (2022), 127595, https://doi.org/10.1016/j.jhazmat.2021.127595.

[2] H. Safardoust-Hojaghan, M. Salavati-Niasari, Degradation of methylene blue as a pollutant with N-doped graphene quantum dot/titanium dioxide nanocomposite, J. Clean. Prod. 148 (2017) 31–36, https://doi.org/10.1016/j.jclepro.2017.01.169.

[3] H. Zhao, G. Li, F. Tian, Q. Jia, Y. Liu, R. Chen, g-C_3N_4 surface-decorated $Bi_2O_2CO_3$ for improved photocatalytic performance: theoretical calculation and photodegradation of antibiotics in actual water matrix, Chem. Eng. J. 366 (2019) 468–479, https://doi.org/10.1016/j.cej.2019.02.088.

[4] S. Chen, M. Zhou, T. Li, W. Cao, Synthesis of Ag-loaded Sb_2WO_6 microsphere with enhanced photocatalytic ability for organic dyes degradations under different light irradiations, J. Mol. Liq. 272 (2018) 27–36, https://doi.org/10.1016/j.molliq.2018.09.044.

[5] Z. Chen, S. Yu, J. Liu, Y. Zhang, Y. Wang, J. Yu, M. Yuan, P. Zhang, W. Liu, J. Zhang, C, F co-doping Ag/TiO_2 with visible light photocatalytic performance toward degrading Rhodamine B, Environ. Res. 232 (2023), 116311, https://doi.org/10.1016/j.envres.2023.116311.

[6] G. Deng, X. Kang, Y. Yang, L. Wang, G. Liu, Skin B/N-doped anatase TiO_2 {001} nanoflakes for visible-light photocatalytic water oxidation, J. Colloid Interfaces Sci. (2023), https://doi.org/10.1016/j.jcis.2023.06.046.

[7] S. Li, M. Cai, Y. Liu, C. Wang, K. Lv, X. Chen, S-Scheme photocatalyst TaON/Bi_2WO_6 nanofibers with oxygen vacancies for efficient abatement of antibiotics and Cr(VI): Intermediate eco-toxicity analysis and mechanistic insights, Chin. J. Catal. 43 (2022) 2652–2664, https://doi.org/10.1016/S1872-2067(22)64106-8.

[8] S. Li, M. Cai, C. Wang, Y. Liu, Ta_3N_5/CdS core–shell S-scheme heterojunction nanofibers for efficient photocatalytic removal of antibiotic tetracycline and Cr (VI): performance and mechanism insights, Adv. Fiber Mater. 5 (2023) 994–1007, https://doi.org/10.1007/s42765-022-00253-5.

[9] R. Firmansyah, R. Bakri, Y. Yulizar, Enhancement of photocatalytic activity of ZnO by $ZnMoO_4$ compositing under visible light via hydrothermal green synthesis, Inorg. Chem. Commun. (2023), https://doi.org/10.1016/j.inoche.2023.110893.

[10] C. Ding, Z. Li, W. Tan, H. Li, J. Ma, Z. Chen, Y. Tao, Y. Qin, Y. Kong, 3D graphene aerogels/Sb_2WO_6 hybrid with enhanced photocatalytic activity under UV- and visible-light irradiation, Synth. Met. 246 (2018) 137–143, https://doi.org/10.1016/j.synthmet.2018.10.010.

[11] J. Huang, Y. Kang, J.A. Liu, R. Chen, T. Xie, Z. Liu, X. Xu, H. Tian, L. Yin, F. Fan, L. Wang, G. Liu, Selective exposure of robust perovskite layer of aurivillius-type compounds for stable photocatalytic overall water splitting, Adv. Sci. (2023), e2302206, https://doi.org/10.1002/advs.202302206.

[12] Y. Zhang, D. Liu, Y. Zhang, Y. Qian, C. Li, Z. Qu, R. Xu, Q. Wei, Highly sensitive photoelectrochemical neuron specific enolase analysis based on cerium and silver Co-Doped Sb_2WO_6, Biosens. Bioelectron. 203 (2022), 114047, https://doi.org/10.1016/j.bios.2022.114047.

[13] S.P. Keerthana, R. Yuvakkumar, P. Senthil Kumar, G. Ravi, S.I. Hong, D. Velauthapillai, Investigation of PEG directed Sb_2WO_6 for dyes removal from wastewater, Chemosphere 291 (2022), 132677, https://doi.org/10.1016/j.chemosphere.2021.132677.

[14] D. Karmakar, S. Datta, D. Jana, Combined theoretical and experimental study of the electronic and optical property of Sb_2WO_6, J. Alloy. Compd. 881 (2021), https://doi.org/10.1016/j.jallcom.2021.160586.

[15] Y. Wang, K. Wang, J. Wang, X. Wu, G. Zhang, Sb_2WO_6/BiOBr 2D nanocomposite S-scheme photocatalyst for NO removal, J. Mater. Sci. Technol. 56 (2020) 236–243, https://doi.org/10.1016/j.jmst.2020.03.039.

[16] S.-P. Hu, C.-Y. Xu, F.-X. Ma, L. Cao, L. Zhen, Solvothermal synthesis of orthorhombic Sb_2WO_6 hierarchical structures and their visible-light-driven photocatalytic activity, Dalton Trans. 43 (2014) 8439–8445, https://doi.org/10.1039/c3dt53561d.

[17] H. Wang, D. Yong, S. Chen, S. Jiang, X. Zhang, W. Shao, Q. Zhang, W. Yan, B. Pan, Y. Xie, Oxygen-vacancy-mediated exciton dissociation in BiOBr for boosting charge-carrier-involved molecular oxygen activation, J. Am. Chem. Soc. 140 (2018) 1760–1766, https://doi.org/10.1021/jacs.7b10997.

[18] X. Jin, C. Lv, X. Zhou, C. Zhang, Q. Meng, Y. Liu, G. Chen, Molecular adsorption promotes carrier migration: key step for molecular oxygen activation of defective $Bi_4O_5I_2$, Appl. Catal. B: Environ. 226 (2018) 53–60, https://doi.org/10.1016/j.apcatb.2017.12.008.

[19] G. Liu, L. Wang, B. Wang, X. Zhu, J. Yang, P. Liu, W. Zhu, Z. Chen, J. Xia, Synchronous activation of Ag nanoparticles and BiOBr for boosting solar-driven CO_2 reduction, Chin. Chem. Lett. 34 (2023), https://doi.org/10.1016/j.cclet.2022.107962.

[20] W. Gao, G. Li, Q. Wang, L. Zhang, K. Wang, S. Pang, G. Zhang, L. Lv, X. Liu, W. Gao, L. Sun, Y. Xia, Z. Ren, P. Wang, Ultrathin porous Bi_2WO_6 with rich oxygen vacancies for promoted adsorption-photocatalytic tetracycline degradation, Chem. Eng. J. 464 (2023), 142694, https://doi.org/10.1016/j.cej.2023.142694.

[21] Y. Shen, C. Ren, L. Zheng, X. Xu, R. Long, W. Zhang, Y. Yang, Y. Zhang, Y. Yao, H. Chi, J. Wang, Q. Shen, Y. Xiong, Z. Zou, Y. Zhou, Room-temperature photosynthesis of propane from CO_2 with Cu single atoms on vacancy-rich TiO_2, Nat. Commun. 14 (2023) 1117, https://doi.org/10.1038/s41467-023-36778-5.

[22] H. Wang, C. Cao, D. Li, Y. Ge, R. Chen, R. Song, W. Gao, X. Wang, X. Deng, H. Zhang, B. Ye, Z. Li, C. Li, Achieving high selectivity in photocatalytic oxidation of toluene on amorphous BiOCl nanosheets coupled with TiO_2, J. Am. Chem. Soc. 145 (2023) 16852–16861, https://doi.org/10.1021/jacs.3c05237.

[23] X. Kong, Y. Xu, Z. Cui, Z. Li, Y. Liang, Z. Gao, S. Zhu, X. Yang, Defect enhances photocatalytic activity of ultrathin TiO_2 (B) nanosheets for hydrogen production by plasma engraving method, Appl. Catal. B: Environ. 230 (2018) 11–17, https://doi.org/10.1016/j.apcatb.2018.02.019.

[24] U. Rafiq, O. Mehraj, S. Lone, M. Wahid, K. Majid, Solvothermal synthesis of Ag_2WO_4/Sb_2WO_6 heterostructures for enhanced charge transfer properties and efficient visible-light-driven photocatalytic activity and stability, J. Environ. Chem. Eng. 8 (2020), https://doi.org/10.1016/j.jece.2020.104301.

[25] B. Wang, J. Zhao, H. Chen, Y.-X. Weng, H. Tang, Z. Chen, W. Zhu, Y. She, J. Xia, H. Li, Unique Z-scheme carbonized polymer dots/$Bi_4O_5Br_2$ hybrids for efficiently boosting photocatalytic CO_2 reduction, Appl. Catal. B: Environ. 293 (2021), https://doi.org/10.1016/j.apcatb.2021.120182.

[26] P. Wang, S. Xie, Y. She, W. Fan, M.K.H. Leung, H. Wang, Microwave-hydrothermal synthesis of hierarchical Sb_2WO_6 nanostructures as a new anode material for sodium storage, ChemistrySelect 4 (2019) 1078–1083, https://doi.org/10.1002/slct.201803284.

[27] Y. Shi, H. Wang, Z. Wang, T. Wu, Y. Song, B. Guo, L. Wu, Pt decorated hierarchical Sb_2WO_6 microspheres as a surface functionalized photocatalyst for the visible-

light-driven reduction of nitrobenzene to aniline, J. Mater. Chem. A 8 (2020) 18755–18766, https://doi.org/10.1039/d0ta06099b.
[28] J. Yang, X. Zhu, Q. Yu, M. He, W. Zhang, Z. Mo, J. Yuan, Y. She, H. Xu, H. Li, Multidimensional In_2O_3/In_2S_3 heterojunction with lattice distortion for CO_2 photoconversion, Chin. J. Catal. 43 (2022) 1286–1294, https://doi.org/10.1016/S1872-2067(21)63954-2.
[29] W. Huo, X. Dong, J. Li, M. Liu, X. Liu, Y. Zhang, F. Dong, Synthesis of Bi_2WO_6 with gradient oxygen vacancies for highly photocatalytic NO oxidation and mechanism study, Chem. Eng. J. 361 (2019) 129–138, https://doi.org/10.1016/j.cej.2018.12.071.
[30] B. Wang, W. Zhang, G. Liu, H. Chen, Y.X. Weng, H. Li, P.K. Chu, J. Xia, Excited electron-rich $Bi^{(3-x)+}$ sites: a quantum well-like structure for highly promoted selective photocatalytic CO_2 reduction performance, Adv. Funct. Mater. 32 (2022), https://doi.org/10.1002/adfm.202202885.
[31] L. Chen, Y. Chao, X. Li, G. Zhou, Q. Lu, M. Hua, H. Li, X. Ni, P. Wu, W. Zhu, Engineering a tandem leaching system for the highly selective recycling of valuable metals from spent Li-ion batteries, Green Chem. 23 (2021) 2177–2184, https://doi.org/10.1039/d0gc03820b.
[32] X. Hu, J. Wang, J. Wang, Y. Deng, H. Zhang, T. Xu, W. Wang, β particles induced directional inward migration of oxygen vacancies: surface oxygen vacancies and interface oxygen vacancies synergistically activate PMS, Appl. Catal. B: Environ. 318 (2022), https://doi.org/10.1016/j.apcatb.2022.121879.
[33] S. Li, C. Wang, K. Dong, P. Zhang, X. Chen, X. Li, MIL-101(Fe)/BiOBr S-scheme photocatalyst for promoting photocatalytic abatement of Cr(VI) and enrofloxacin antibiotic: performance and mechanism, Chin. J. Catal. 51 (2023) 101–112, https://doi.org/10.1016/S1872-2067(23)64479-1.
[34] Y. Ren, Y. Li, X. Wu, J. Wang, G. Zhang, S-scheme $Sb_2WO_6/g\text{-}C_3N_4$ photocatalysts with enhanced visible-light-induced photocatalytic NO oxidation performance, Chin. J. Catal. 42 (2021) 69–77, https://doi.org/10.1016/S1872-2067(20)63631-2.
[35] B. Wang, X. Zhu, F. Huang, Y. Quan, G. Liu, X. Zhang, F. Xiong, C. Huang, M. Ji, H. Li, P.K. Chu, J. Xia, Porous edge confinement: High carrier potential and low activation energy barrier synergistically boosting the efficiency of selective photocatalytic CO_2 conversion, Appl. Catal. B: Environ. 325 (2023), https://doi.org/10.1016/j.apcatb.2022.122304.
[36] J. Liu, S. Zhu, B. Wang, R. Yang, R. Wang, X. Zhu, Y. Song, J. Yuan, H. Xu, H. Li, A candy-like photocatalyst by wrapping Co, N-co-doped hollow carbon sphere with ultrathin mesoporous carbon nitride for boosted photocatalytic hydrogen evolution, Chin. Chem. Lett. 34 (2023), https://doi.org/10.1016/j.cclet.2022.107749.
[37] J. Liu, R. Wang, B. Wang, M. Zheng, R. Yang, X. Zhu, Y. Song, M. Cheng, H. Xu, H. Li, An all-organic spatial structure composed of perylene diimide/mesoporous graphitic carbon nitride for high efficiency photocatalysis, Appl. Surf. Sci. 605 (2022), https://doi.org/10.1016/j.apsusc.2022.154625.
[38] J. Feng, D. Zhang, H. Zhou, M. Pi, X. Wang, S. Chen, Coupling P nanostructures with P-doped $g\text{-}C_3N_4$ as efficient visible light photocatalysts for H_2 evolution and RhB degradation, ACS Sustain. Chem. Eng. 6 (2018) 6342–6349, https://doi.org/10.1021/acssuschemeng.8b00140.
[39] S. Li, R. Yan, M. Cai, W. Jiang, M. Zhang, X. Li, Enhanced antibiotic degradation performance of $Cd_{0.5}Zn_{0.5}S/Bi_2MoO_6$ S-scheme photocatalyst by carbon dot modification, J. Mater. Sci. Technol. 164 (2023) 59–67, https://doi.org/10.1016/j.jmst.2023.05.009.
[40] N. Gou, W. Yang, S. Gao, Q. Li, Incorporation of ultrathin porous metal-free graphite carbon nitride nanosheets in polyvinyl chloride for efficient photodegradation, J. Hazard. Mater. 447 (2023), 130795, https://doi.org/10.1016/j.jhazmat.2023.130795.
[41] G. Liu, M. Liao, Z. Zhang, H. Wang, D. Chen, Y. Feng, Enhanced photodegradation performance of Rhodamine B with $g\text{-}C_3N_4$ modified by carbon nanotubes, Sep. Purif. Technol. 244 (2020), https://doi.org/10.1016/j.seppur.2020.116618.

Low-temperature plasma-induced porous Sb_2WO_6 microspheres with rich oxygen vacancies to promote high-performance photocatalytic activity

Qichang Peng[a1], Qingdong Ruan[b1], Bin Wang[a,b1], Jinyuan Liu[a,b], Chao Huang[b], Xingwang Zhu[c], Dan Li[b], Liangliang Liu[b], Yinchuan Wang[b], Xiaolin Zhang[b], Jia Yan[a], Paul K. Chu[b*], Hui Xu[a*]*

[a] *School of Chemistry and Chemical Engineering, Institute for Energy Research, Jiangsu University, 301 Xuefu Road, Zhenjiang 212013, China*

[b] *Department of Physics, Department of Materials Science and Engineering, and Department of Biomedical Engineering, City University of Hong Kong, Tat Chee Avenue, Kowloon, Hong Kong, China*

[c] *College of Environmental Science and Engineering, Yangzhou University, Yangzhou 225009, China*

** Corresponding authors: jyliu@ujs.edu.cn (J. Liu), paul.chu@cityu.edu.hk; xh@ujs.edu.cn (H. Xu).*

[1] *These authors contributed equally to this work.*

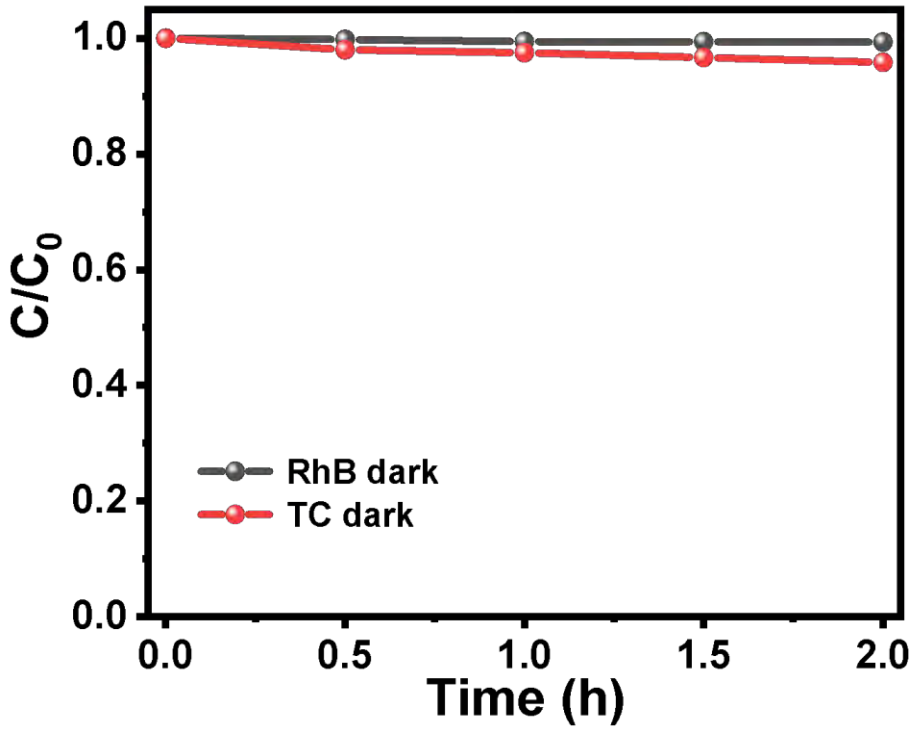

Figure S1. Reaction profile of RhB and TC in the dark in the presence of the photocatalyst.

Table S1. The performance improvement of different types photocatalysts in the field of photocatalytic degradation.

Photocatalyst	Organic Pollutant	Light Source	Rate Constant	Multiple/After modification	Reference
K-gC_3N_4	RhB	Vis	0.0029 min^{-1}	/	[1]
ACB-K-gC_3N_4(1：2)	RhB	Vis	0.0119 min^{-1}	4.10	
Bi_2WO_6	RhB	Vis	0.00531 min^{-1}	/	[2]
SBB	RhB	Vis	0.01461 min^{-1}	2.8	
CdS	RhB	Vis	0.05833 min^{-1}	/	[3]
$SRP_{0.03}$/CdS	RhB	Vis	0.1034 min^{-1}	1.8	
TiO_2	RhB	Vis	0.00109 min^{-1}	/	[4]
5%CODs+TiO_2	RhB	Vis	0.01574 min^{-1}	14.4	
$BiVO_4$	RhB	Vis	0.00290 min^{-1}	/	[5]
GO/BV	RhB	Vis	0.003828 min^{-1}	1.31	
ZnO	RhB	Vis	0.0047 min^{-1}	/	[6]
ZnO-rGO	RhB	Vis	0.0247 min^{-1}	5.26	
BOC	RhB	Vis	0.028 min^{-1}	/	[7]
BOC-CTAB	RhB	Vis	0.181 min^{-1}	6.46	
BOB	RhB	Vis	0.074 min^{-1}	/	[8]
BOB@NCQDs-5	RhB	Vis	0.187 min^{-1}	2.53	
$Bi2MoO_6$	RhB	Vis	0.0049 min^{-1}	/	[9]
BC-1	RhB	Vis	0.0352 min^{-1}	7.18	
Sb_2WO_6	RhB	Vis	0.00191 min^{-1}	/	[10]
1% CQDs/Sb_2WO_6	RhB	Vis	0.01346 min^{-1}	7.04	
Sb_2WO_6	RhB	Vis	0.03 h^{-1}	/	This work
OV-Sb_2WO_6-20	RhB	Vis	0.27 h^{-1}	9	

Reference

[1] T. Wang, J. Zheng, J. Cai, Q. Liu, X. Zhang, Visible-light-driven photocatalytic degradation of dye and antibiotics by activated biochar composited with K^+ doped g-C_3N_4: Effects, mechanisms, actual wastewater treatment and disinfection, Sci Total Environ. 839 (2022) 155955. http://doi.org/10.1016/j.scitotenv.2022.155955.

[2] X. Xu, G. Liu, L. Li, N. Shan, B. Wang, M. Ji, J. Xia, H. Li, In-situ construction of Sn-doped BiOCl/Bi_2WO_6 heterojunction for excellent organic pollutants degradation: Insight into performance and mechanism, Appl Surf Sci. 635 (2023) 157512. https://doi.org/10.1016/j.apsusc.2023.157512.

[3] Ahmed Th. Abdulghaffar, Gomaa Khabiri b, Hemdan S.H. Mohamed, A novel SRP/CdS heterostructure hollow nanospheres for outstanding photocatalytic performance, Sep Purif Technol. 326 (2023) 124813. https://doi.org/10.1016/j.seppur.2023.124813.

[4] S. Tong, J. Zhou, L. Ding, Ch. Zhou, Y. Liu, S. Li, J. Meng, S. Zhu, S. Chatterjee, F. Liang, Preparation of carbon quantum dots/TiO2 composite and application for enhanced photodegradation of rhodamine B, Colloids Surf. A: Physicochem. Eng. Asp.. 648 (2022) 129342. https://doi.org/10.1016/j.colsurfa.2022.129342.

[5] A.I. Moral-Rodríguez, M. Quintana, R. Leyva-Ramos, H.J. Ojeda-Galvan, S. Oros-Ruiz, R.D. Peralta-Rodríguezf, E. Mendoza-Mendoza, Novel and green synthesis of $BiVO_4$ and GO/$BiVO_4$ photocatalysts for efficient dyes degradation under blue LED illumination, Ceram Int. 48 (2022) 1264–1276. https://doi.org/10.1016/j.ceramint.2021.09.211.

[6] W. Yein, Q. Wang, X. Feng, Y. Li, X. Wu, Enhancement of photocatalytic performance in sonochemical synthesized ZnO–rGO nanocomposites owing to effective interfacial interaction, Environ Chem Lett,16 (2018) 251–264. https://doi.org/10.1007/s10311-017-0651-1.

[7] T. Guo, X. Fan, X. Jiang, Y. Qi, J. Du, A. Zhang, H. Wang, Engineering shape of BiOCl nanosheets with improved visible-light response for superior photocatalytic degradation of Rhodamine B, J Alloy Compd, 948 (2023) 169586. https://doi.org/10.1016/j.jallcom.2023.169586.

[8] Y. Qi, J. Zhao, H. Wang, A. Zhang, J. Li, M. Yan, T. Guo, Shaddock peel-derived N-doped carbon quantum dots coupled with ultrathin BiOBr square na

nosheets with boosted visible light response for high-efficiency photodegradation of RhB, Environ Pollut, 325 (2023) 121424. https://doi.org/10.1016/j.envpol.2023.121424.

[9] Q. Gao, K. Sun, Y. Cui, S. Wang, C. Liu, B. Liu，In situ growth of 2D/3D Bi_2MoO_6/CeO_2 heterostructures toward enhanced photodegradation and Cr(VI) reduction，Sep Purif Technol， 285 (2022) 120312. https://doi.org/10.1016/j.seppur.2021.120312.

[10] W. Li, Z. Wang, Y. Li, J. Ghasemi, J. Li, G. Zhang, Visible-NIR light-responsive 0D/2D CQDs/Sb_2WO_6 nanosheets with enhanced photocatalytic degradation performance of RhB: Unveiling the dual roles of CQDs and mechanism study, J Hazard Mater, 424 (2022) 127595. https://doi.org/10.1016/j.jhazmat.2021.127595.